

A westward extension of the warm pool leads to a westward extension of the Walker circulation, drying eastern Africa

A. Park Williams · Chris Funk

Received: 3 June 2010 / Accepted: 21 December 2010 / Published online: 4 January 2011
© The Author(s) 2010. This article is published with open access at Springerlink.com

Abstract Observations and simulations link anthropogenic greenhouse and aerosol emissions with rapidly increasing Indian Ocean sea surface temperatures (SSTs). Over the past 60 years, the Indian Ocean warmed two to three times faster than the central tropical Pacific, extending the tropical warm pool to the west by $\sim 40^\circ$ longitude ($>4,000$ km). This propensity toward rapid warming in the Indian Ocean has been the dominant mode of interannual variability among SSTs throughout the tropical Indian and Pacific Oceans (55°E – 140°W) since at least 1948, explaining more variance than anomalies associated with the El Niño–Southern Oscillation (ENSO). In the atmosphere, the primary mode of variability has been a corresponding trend toward greatly increased convection and precipitation over the tropical Indian Ocean. The temperature and rainfall increases in this region have produced a westward extension of the western, ascending branch of the atmospheric Walker circulation. Diabatic heating due to increased mid-tropospheric water vapor condensation elicits a westward atmospheric response that sends an easterly flow of dry air aloft toward eastern Africa. In recent decades (1980–2009), this response has suppressed convection over tropical eastern Africa, decreasing precipitation during the ‘long-rains’ season of March–June. This trend toward drought contrasts with projections of increased rainfall in eastern Africa and more ‘El Niño-like’ conditions globally by the Intergovernmental Panel on Climate Change. Increased Indian Ocean SSTs appear likely to continue to strongly modulate the Warm Pool circulation, reducing precipitation in eastern Africa, regardless of whether the projected trend in ENSO is

realized. These results have important food security implications, informing agricultural development, environmental conservation, and water resource planning.

Keywords East Africa · Indian Ocean · Precipitation · Drought · Tropical warm pool · Climate change

1 Introduction

An estimated 17.5 million people are food insecure in Kenya, Ethiopia, and Somalia, and the US government has spent over \$1.1 billion on food aid in these countries since 2009.¹ Food balance modeling suggests that this insecurity stems (in part) from stagnating agricultural development, population growth, and recent drought (Funk et al. 2008; Funk and Brown 2009); which has been linked to human-caused warming in the Indian Ocean (Funk et al. 2005, 2008; Verdin et al. 2005). This warming appears to have had a large impact on eastern African rainfall from March to June (MAMJ, Funk et al. 2008; Funk and Verdin 2009). This season is known as the ‘long rains’ in Kenya and the ‘Belg’ rains in Ethiopia. In this paper, we show that a suite of observational datasets indicate a westward extension of the tropical warm pool into the Indian Ocean during MAMJ; this extension appears to be extending the zonally overturning atmospheric Walker circulation in a westward direction. While there appear to be many factors that govern interannual variability in east African long-rains precipitation, convective activity during MAMJ has steadily declined in eastern Africa for the past 30 years as the

A. P. Williams (✉) · C. Funk
Geography Department, University of California,
Santa Barbara, Santa Barbara, CA 93101, USA
e-mail: williams@geog.ucsb.edu

¹ http://www.usaid.gov/our_work/humanitarian_assistance/ffp/where_wework.html. Estimates based upon data from July 2010.

convective branch of the Walker circulation has become more active over the Indian Ocean.

Diagnoses of the reasons behind the declining long-rains precipitation have been elusive because the factors governing the interannual variability of long-rains precipitation totals are complicated and not well understood (Ogallo 1988; Camberlin and Philippon 2002; Pohl and Camberlin 2006b). While short-rains (October–December) precipitation is strongly influenced by the ENSO phenomenon (Ogallo 1988; Hastenrath et al. 1993; Nicholson and Kim 1997; Nicholson and Selato 2000) and the Indian Ocean Dipole (IOD, Saji et al. 1999; Abram et al. 2008), long-rains precipitation does not correlate well with ENSO or IOD indices (Pohl and Camberlin 2006b). Correlations are also weak between long rains and SST in any one region (Ogallo 1988; Rowell et al. 1994).

The poor relationships with SST patterns suggest that interannual variability in long-season precipitation must be associated with internal atmospheric variability (Camberlin and Philippon 2002). In search of an atmospheric mechanism influencing interannual variability of long rains, Pohl and Camberlin (2006a, b) implicated the Madden-Julian Oscillation (MJO, Madden and Julian 1971, 1972, 1994), where wet conditions during the early part of the long rains are associated with high-amplitude MJO conditions. Key characteristics of high-amplitude MJO conditions during MAMJ are westerly wind anomalies throughout the atmospheric column above tropical Africa and overturning circulation anomalies over the tropical Indian Ocean with westerly anomalies in the upper troposphere, downward anomalies over the Maritime Continent, and easterly anomalies in the lower troposphere. These conditions presumably allow for increased westerly moisture transports across the interior of Africa, somewhat increased easterly transports from the Indian Ocean, and reduced subsidence over eastern Africa (Pohl and Camberlin 2006a). Curiously, however, the statistical correlation between MJO amplitude and long-rains precipitation lost considerable strength after the 1980s (Pohl and Camberlin 2006b).

More recently, Funk et al. (2008) suggested that long-established interannual relationships between large-scale climate variability and long-rains precipitation are being altered due to warming within the south central Indian Ocean. Funk et al. suggest that warming near the western edge of the tropical Pacific-Indian Ocean warm pool tends to increase deep atmospheric convection over the Indian Ocean. This increased convection over the Indian Ocean is associated with increased subsidence and reduced rainfall across eastern Africa. Variations in temperature and convection in the Indian Ocean region modulate, and are modulated by, the tropical Pacific Walker Cell, which is characterized by low-level easterly wind flow from the

relatively cool eastern equatorial Pacific toward the warmer western equatorial Pacific and return flow within the upper troposphere. Gill (1980, 1982) shows that this very large circulation can be considered as a steady-state solution to the shallow water wave equations when forced with a diabatic heating (latent heat release) term centered over the warm pool. This solution has two components, a long eastward Kelvin wave response, associated with the easterly Pacific tradewinds, and a shorter Rossby wave response that brings dry air down across eastern Africa. Indeed, the interannual analysis by Pohl and Camberlin (2006b) found that, from 1979 to 2001, anomalously high convective activity over the center of the warm-pool region (Maritime Continent) was associated with reduced convective activity over eastern Africa during the long-rains season. Thus, a change in the behavior of the western, ascending branch of the Walker cell would presumably initiate a change in the mean vertical atmospheric movement over eastern Africa.

At present, there is great interest and debate regarding how continued global warming would impact the Pacific Walker Cell, and its principal interannual variation (ENSO). One reason for uncertainty is the fact that anthropogenic changes in the Pacific climate will be intermingled with natural internal climate variations. These shifts vary on ~ 20 -years time scales, and a large change before and after the 1970s has been well-documented (Graham 1994; Zhang et al. 1997; Kirtman and Schopf 1998). All models used in the 21st century climate model experiments performed for the Intergovernmental Panel on Climate Change (IPCC) 4th Assessment Report (AR4) predict that tropospheric warming will lead to a weakening of tropical circulation (Held and Soden 2006; Vecchi and Soden 2007). In short, this is because relatively rapid warming in the middle and upper troposphere are projected to cause tropospheric water vapor content to increase substantially more than precipitation within the tropics. This imbalance is expected to slow the overall vertical mass-movement of the tropical troposphere (Knutson and Manabe 1995; Held and Soden 2006).

Models generally project that decreased vertical circulation within the tropical atmosphere should weaken the tropical Walker circulation (Knutson and Manabe 1995; Held and Soden 2006; Vecchi et al. 2006; Lu et al. 2007). A weakened Walker circulation is projected to resemble a more “El Niño-like” climate with decreased convection over the western tropical Pacific and decreased subsidence over the eastern tropical Pacific and eastern tropical Africa (Vecchi and Soden 2007). Notably, the weakened, more “El Niño-like” Walker circulation only describes the mean state of the projected Walker circulation, not the proportion of El Niño events compared to La Niña events (Solomon et al. 2007; Vecchi and Soden 2007). It is also important to

note that the IPCC AR4 presents a mixed view on changes in ENSO (Christiansen et al. 2007; Meehl et al. 2007), suggesting that substantial uncertainty remains in how precipitation is likely to change in locations where precipitation is impacted by the state of the ENSO cycle.

Forecasts of decreased tropical Walker circulation are at odds with several observational studies that noted trends indicating an *intensified* Walker circulation during the latter half of the 20th century. For example, Minobe (2005) found increased convection over the Maritime Continent and increased downward vertical anomalies over the central equatorial Pacific Ocean from 1948 through 2002 in NCEP/NCAR reanalysis wind divergence data. Compo and Sardeshmukh (2010) removed the impact of ENSO from the HadISST record of sea surface temperature (SST) anomalies and found that the remaining (ENSO-unrelated) component of the observed trend from 1949 to 2006 is above $1.2^{\circ}\text{C}/\text{century}$ throughout much of the warm-pool region, and below $-0.4^{\circ}\text{C}/\text{century}$ in much of the cold-tongue region that extends from the South American equatorial Pacific coast westward along the equator. Consistent with this study, Cane et al. (1997) observed 20th century cooling in the cold-tongue region and a strengthening of the zonal SST gradient between the cold tongue and the warm pool. These studies suggest that in the absence of ENSO variability, there has been a multi-decade intensification of surface easterlies across the equatorial Pacific Ocean, in agreement with an intensified Walker circulation, as suggested by the modeling study presented by Clement et al. (1996). Considering more recent time periods, Chen et al. (2002) analyzed satellite imagery from 1985 through 2000 and found that long-wave radiation emitted to space decreased in areas associated with tropical Hadley and Walker convection, and long-wave emissions increased in areas associated with subsidence. Chen et al. invoked an intensification of Hadley and Walker circulations, concluding that outgoing terrestrial radiation increased where there was decreased cloud cover and conversely, decreased where there was increased cloud cover. Quan et al. (2004) corroborated these results using a modeling approach; when forced with observed monthly SSTs from 1950 through 1999, the ECHAM-3 GCM simulated increased precipitation over the Indian Ocean, and no change in precipitation over the equatorial central Pacific Ocean. All these studies suggest the Walker circulation is not weakening.

In this study, we use principal component analysis (PCA) of a suite of climate datasets to provide evidence for a westward extension, not a weakening, of the tropical Walker circulation during east Africa's long rains season. We propose that this westward extension is the result of an extension of the western edge of the tropical warm pool in the Indian Ocean. We contrast this observational trend with

Walker-circulation trends simulated by an ensemble of GCMs. Finally, we suggest that the westward extension of Walker circulation has likely contributed to increased subsidence and decreased MAMJ rainfall in eastern Africa. This result is contrary to the AR4 findings, for which 18 of 21 models evaluated for the IPCC AR4 agree upon increased precipitation in eastern Africa (Christiansen et al. 2007). The IPCC AR4 therefore states that the increased precipitation is 'likely'. Presenting a countervailing view, Funk and Brown (2009) showed that when constrained by observed SSTs from 1980 through 2000, rainfall estimates by an ensemble of 10 GCMs used for the IPCC AR4 were actually *anti-correlated* with observed long-season rainfall totals in eastern Africa. Nonetheless, the projections of increased rainfall in eastern tropical Africa are taken seriously by food aid agencies, and hundreds of millions of dollars in development aid for agriculture, environmental conservation, and water resource planning are predicated on such uncertain IPCC projections. If the climate continues to tilt toward an intensified Walker circulation, or a westward extension of its western branch, rainfall should continue to decrease in the most food insecure region of the world.

2 Materials and methods

The purpose of this study is to marshal numerous data sources to evaluate two important scientific questions: what drives interannual variations in the Indo-Pacific warm pool region, and how do these variations impact rainfall in eastern Africa? We pursue the first question via (1) a principal component analysis of Indo-Pacific reanalysis fields, followed by (2) a corresponding evaluation of additional climate observations and climate change simulations. Having identified a dominant mode of warming-related Indo-Pacific climate variation, we then proceed to link this mode with station-based observations of declining rainfall in eastern Africa, and variations of the 500 hPa Meridional Height Gradient (MHG) across the Indian Ocean.

2.1 Principal component analysis of reanalysis fields

PCA is a useful way to identify climate processes and trends that are coherent among many datasets (von Storch and Zwiers 1999). We used PCA of tropical reanalysis data to identify and summarize the two primary modes of interannual MAMJ variability in the tropical tropospheric circulation overlying the tropical (20°S – 20°N) Indian and Pacific Oceans (55°E – 140°W). Extensive sensitivity testing indicated that the results of the PCA were not strongly impacted by the location of the eastern boundary of this

region (i.e., the amount of the central and eastern tropical Pacific included). Four variables were analyzed: 2 m air temperature, precipitation totals, zonal wind velocity, and vertical velocity (omega). Temperature and precipitation datasets were surface grids between 20°S and 20°N, 55°E and 140°W. Zonal and vertical velocity datasets were also between 55°E and 140°W, but these data were three dimensional with 17 and 12 geopotential height levels, respectively. We converted these to two dimensional vertical profile fields by averaging values between 10°S and 10°N.

We converted records of temperature, zonal wind velocity, and vertical velocity into z-scores (by subtracting the mean and dividing by the standard deviation), and records of precipitation totals to anomalies. Sensitivity tests indicated that the results of the PCA were not impacted substantially by the use of 2-m temperature over SST, nor by the use of precipitation anomalies rather than z-scores. They were also not impacted substantially by the inclusion or exclusion of precipitation data. This indicates that the results of the PCA are robust despite the notoriously high uncertainty of precipitation estimates during the pre-satellite era (pre-1979). The PCA was then done in two steps. In the first step, we calculated four independent PCAs based respectively on the air temperature, zonal wind, vertical velocity, and rainfall data. For each variable, we then identified the three principal component (PC) time series sharing the most variability with the original data. These three time-series captured 42–68% of the variance among the four variables. We then combined these three time series from each variable into one matrix (12 variables by 62 years) and weighted the mean and variance of each time series by the fraction of variability that it shared with its original data. We conducted a second PCA on these 12 variance adjusted PC time series. This produced 12 new PC time series, each representing some component of the large-scale, multi-variate climate of the tropical Indian and Pacific Ocean area.

For each variable, we calculated a correlation map showing the spatial relationships between the original climate data and each of the first two new PC time series. We interpreted these correlation maps subjectively and determined how each of the first two PC time series related to well known large-scale climate phenomena.

We tested the robustness of the results of the PCA by repeating this procedure using three alternate climate datasets and comparing the resultant PC time series to those calculated using the NCEP/NCAR reanalysis data. In one repetition, we used gridded reanalysis data for the same four variables, produced by the European Centre for Medium-Range Weather Forecasts (ECMWF) ERA-40 project (accessed online at <http://www.data.ecmwf.int/data/>). This dataset only extended from 1958 through 2002. In the

second repetition of the PCA, we used radiosonde data from 1979 through 2009 from 19 countries that are located within the tropical Indian-Pacific Ocean area of 20°S–20°N, 55°E–140°W. In this analysis, only surface temperature and zonal wind-profile data were used. See the appendix for further description of the radiosonde data. Finally, for a more direct comparison between the radiosonde and NCEP/NCAR data, we repeated the PCA on NCEP/NCAR data using only the same variables and temporal coverage as were used in the radiosonde analysis. The three climate datasets used in this analysis are not independent, as radiosonde measurements are used to constrain the climate models used to produce both reanalysis datasets.

To further test that the PC time series represent true climate processes and not artifacts of reanalysis and/or radiosonde data, we considered five new global precipitation products that are based upon satellite and/or station data. These products are the (1) Global Precipitation Climatology Project (GPCP) version 2.1 combined precipitation dataset (Huffman et al. 1997, 2009; Adler et al. 2003), (2) NCEP-DOE Reanalysis 2 (NCEP II, Kanamitsu et al. 2002), (3) CPC Merged Analysis of Precipitation (CMAP, Xie and Arkin 1997), (4) CPC Precipitation Reconstruction (CPC PREC, ftp.cpc.ncep.noaa.gov/precip/50yr/land_ocean), and (5) NOAA merged precipitation reconstruction (MergPr, Smith et al. 2010).

2.2 Comparison of reanalysis and modeled climate data

A primary goal of this study was to identify whether variability in the global mean surface temperature has impacted the Walker-like (zonal) circulation of the tropical atmosphere overlying the Indian and Pacific Oceans. Because changes in the Walker circulation should be accompanied by changes in the hydrological cycle throughout the tropics (Diaz and Markgraf 1992; Webster 1998), we wished to determine whether observed changes in the Walker circulation are represented among the 21 GCMs used by the IPCC AR4 to develop projections of regional changes in rainfall. To do this, we compared observational records of MAMJ climate data to 84 runs of modeled 20th century climate data produced by 21 GCMs as part of phase 3 of the Coupled Model Intercomparison Project (CMIP3) 20th century climate experiment (20c3 m) for the IPCC AR4. These models are described by Randall et al. (2007) and listed in the legend of Fig. 5. All model data were provided by the World Climate Research Programme Multi-Model Database (<https://www.esg.llnl.gov/8443/about/overviewPage.do>).

Model runs within the CMIP3 20c3m were driven entirely by external forcing such as solar insolation and the

greenhouse effect. This means that the timing of high-frequency variability events (e.g., ENSO cycles) within 20c3m records do not necessarily agree with the observational record. All model runs do, however, simulate a 20th century increase in global mean tropospheric temperature. Within each modeled and observational record, we evaluated how specific characteristics of the MAMJ Indian-Pacific Walker circulation are related to global mean surface temperature. We then compared the modeled and observed relationships between MAMJ Walker circulation and global mean temperature.

To make this comparison, we considered the four reanalysis variables discussed above in Sect. 2.1. For each variable we chose two regions with historically contrasting relationships with the intensity of Indian-Pacific Walker circulation during MAMJ. Listed in Table 1 are the four variables, the regions chosen for each variable, and a description of typical climate anomalies during years of anomalously intense Walker circulation in each region.

For temperature, we compared models to several gridded interpolations of observational records. These were the NCEP/NCAR reanalysis of 2 m temperature, NOAA extended SST reanalysis, Kaplan SST reanalysis, GISS surface temperature analysis, ECMWF ERA-40, and Hadley Centre's CRU Air and Marine Temperature Anomalies (HADCRUT3) dataset. For zonal wind velocity, vertical velocity, and precipitation, we compared models to the NCEP/NCAR reanalysis and ECMWF ERA-40 datasets. All observational data besides the ECMWF ERA-40 covered the years 1948 through 2009. The ECMWF ERA-40 ranged from 1958 through 2002. All observational data besides the ECMWF ERA-40 were provided by the same source as the NCEP/NCAR reanalysis: the NOAA Earth System Research Laboratory (ESRL) Physical Sciences Division (PSD), Boulder, Colorado, USA, from their website (<http://www.esrl.noaa.gov/psd>).

To reduce the impact of interannual ENSO variability on Walker circulation and global temperatures, we worked with time series smoothed with a 5-years running mean. This isolated lower-frequency covariant within the datasets related to increasing global temperatures. For each

modeled and observational dataset, we regressed smoothed data against the corresponding smoothed MAMJ mean global surface temperature (the NASA GISS land/sea air temperature estimates). We then calculated regional averages of the slope coefficients for each variable and region listed above. The temporal coverage among models and observational records varied between datasets, as did the long-term means and variability within the data. We therefore standardized all model and observational data and re-expressed them to have the same means and standard deviations as the NCEP/NCAR reanalysis data.

2.3 High quality interpolated precipitation data for eastern Africa

Because reanalysis data do not correlate well with observed precipitation in this region (Funk and Verdin 2003), we use interpolation of a unique set of observational precipitation records as the primary basis for evaluating trends in eastern Africa (Funk et al. 2003, 2007; Funk and Michaelsen 2004; Funk and Verdin 2009). The Climate Hazard Group (CHG) at the University of California, Santa Barbara is closely involved in famine early warning in eastern Africa, and has developed a dense quality controlled gauge dataset for the region, with over 350 stations in Kenya and Ethiopia. Many of these rain gauge observations were purchased from the Ethiopian Meteorological Agency and are not publically available. These stations were combined with gauges from neighboring countries, and quality controlled by hand via visual comparisons with neighbors. The data were then translated into MAMJ totals. Gamma distributions were also fit to each station and used to screen for abnormal values. Means were calculated over the 1960–1989 period and seasonal percent anomalies were estimated by dividing by means. Percent anomalies were then interpolated using kriging, and the data reconverted to millimeters by multiplying against a high resolution climatology (Funk and Verdin 2009). The interpolated precipitation dataset used in this study has 0.1° spatial resolution and is hereon referred to as CHG-CLIM. CHG-CLIM improves upon the estimates of east African rainfall

Table 1 Reanalysis variables evaluated, the geographic regions that they were evaluated in, and the anomalies expected in the case of intensified Walker circulation

Variable	Region	Region boundaries	Walker anomaly
1. 2 m MAMJ temperature	1	10°N–10°S, 180°E–140°W	Cool
	2	10°N–10°S, 55°E–120°E	Warm
2. Zonal wind velocity	1	10°N–10°S, 90–180°E, 400–100 hPa	Positive
	2	10°N–10°S, 90–180°E, 1,000–750 hPa	Negative
3. Vertical velocity	1	10°N–10°S, 180°E–140°W, 850–200 hPa	Downward
	2	0°S–15°S, 60°E–90°E, 850–200 hPa	Upward
4. Precipitation total	1	10°N–10°S, 180°E–140°W	Low
	2	0°S–15°S, 60°E–90°E	High

made by the Global Precipitation Climatology Centre (GPCC) thanks to the substantially higher number of gauges and higher spatial resolution. The spatial resolution is especially important in the Ethiopian Highlands, where a very complex topography causes high heterogeneity in precipitation totals. The high spatial heterogeneity can be problematic because high correlation cannot always be expected among precipitation records from relatively nearby stations. Notably, Dinku et al. (2008) used many of the same Ethiopian Highland station datasets as are used in this study and found very strong agreement with several global gridded precipitation datasets. This contributes to our confidence in the CHG-CLIM product.

2.4 Interannual long-rains variability via meridional height gradient

We used rotated PCA on the standardized CHG-CLIM dataset and identified seven regions in Kenya and Ethiopia where interannual MAMJ precipitation variability is spatially coherent. The number of regions was determined using the Monte Carlo rule-N method (Preisendorfer et al. 1981). Within each region we calculated the mean standardized precipitation record and converted these standardized values to percent of the 30-years mean from 1950 through 1979. We then compared these CHG-CLIM regional records to those produced by the GPCC and the GPCP to demonstrate that all three datasets are in agreement regarding Kenyan and Ethiopian rainfall declines in recent decades.

For evaluation of the large-scale climate processes associated with drought during the long rains, we calculated a single standardized precipitation time series for Kenya and Ethiopia. For this calculation, we excluded all areas where (1) there have not been substantial declines over the past three decades, (2) MAMJ is not the dominant precipitation season, and/or (3) rainfall gauge data are sparse.

We next examined NCEP/NCAR reanalysis moisture transports during MAMJ within the lower troposphere (1,000–700 hPa) on a global scale, focusing on anomalies during the wettest and driest 20% of years in Kenya and Ethiopia. We also calculated how moisture transports and specific humidity have related to the primary modes of climate variability identified in the PCA. We compared the spatial structure of the correlation fields to the spatial patterns during wet and dry years. We complimented this analysis with an analysis of how the PC time series correlate with vertical and zonal wind velocities looking across tropical/northern Africa and the tropical Indian and western Pacific Oceans.

Notably, our main hypothesis is that a western extension of the Walker circulation into the Indian Ocean has begun

to suppress long-rains precipitation, not that interannual variability in Walker circulation is the primary driver of long-rains variability. We therefore concluded our analysis by evaluating whether long-term trends in Walker circulation have discernibly impacted the interannual relationships. To date, the strongest published relationship with long-rains precipitation is with the amplitude of the MJO cycle (Pohl and Camberlin 2006b), as calculated by Wheeler and Hendon (2004). This statistical relationship reflects a positive association between long-rains precipitation and a westerly anomaly in lower- and mid-tropospheric wind velocities across both the southern and northern tropical Indian Ocean regions and all parts of Africa south of the equator. In a set of exploratory analyses, we found that this interannual relationship with long-rains precipitation is even stronger when we consider a driver of these mid-tropospheric westerly anomalies: a weak or reversed gradient between relatively low mid-tropospheric geopotential heights over the center of the warm pool region and relatively high geopotential heights to the north, south, and west of this region. The boundaries of these regions are displayed in Fig. 9a of the results section of this paper, where region A is the northern region spanning across northern Africa, India, and southeast Asia (10°N–25°N, 20°W–110°E); region B is the southern region spanning across southern Africa, the southern tropical/subtropical Indian Ocean, and western Australia (35°S–10°S, 20°W–130°E); and region C is the central centered over the eastern Indian Ocean and Maritime Continent (7.5°S–7.5°N, 70°E–130°E). We define the MHG as

$$\text{MHG} = -0.44H_{Az} - 1.30H_{Bz} + 1.44H_{Cz}. \quad (1)$$

H_{Az} , H_{Bz} , and H_{Cz} represent mean standardized MAMJ 500-hPa height within regions A, B, and C, respectively. In other words, all seasonal records of 500-hPa heights within a region are pre-standardized and then averaged together. The coefficients were determined from a linear multiple regression using H_{Az} , H_{Bz} , and H_{Cz} to estimate long-rains precipitation, where high MHG indicates a weak or reversed gradient and results in high estimated precipitation. MHG correlates with long-rains precipitation with $r = 0.61$ while MJO amplitude correlates with $r = 0.43$. Notably, the correlation coefficient for MHG versus precipitation strengthens to 0.67 when regional boundaries are calculated using contouring methods (not shown).

Finally, we evaluated how the long-established interannual relationship between MHG and long-rains precipitation may be impacted by the westward extension of the Walker circulation. We hypothesized that the westward extension of the Walker circulation has begun to suppress long-rains precipitation during both high and low MHG years. In this analysis, we considered GPCC and CHG-CLIM

precipitation datasets to evaluate long-rains precipitation in Africa because of their long temporal coverage. We also considered MAMJ SSTs (NOAA extended dataset) to compare multi-decadal trends in SSTs compared to the interannual variability associated with MHG.

3 Results

3.1 Principal component analyses

The PCA of NCEP/NCAR reanalysis data revealed that surface temperature, zonal wind velocity, vertical velocity, and precipitation share two primary modes of variability in the tropical Indian and Pacific Ocean area during MAMJ. The first PC time series (PC1) accounts for 57% of the interannual variability among the original 12 PC time series (the first three PCs for each of the four climate variables). Figure 1d shows that this primary mode of variability is tightly coupled with surface warming in the tropical Indian Ocean ($r > 0.8$) and mildly coupled with warming in the Pacific Ocean ($r \sim 0.6$). PC1 also seems to be associated with a trend towards a zonally overturning Walker-like circulation, with an ascending branch centered over the rapidly warming Indian Ocean and a descending branch over the more slowly warming central tropical Pacific, between 180°W and 150°W (Fig. 1c). According to the NCEP/NCAR reanalysis, these ascending and descending branches have been accompanied by increased precipitation over the Indian Ocean and decreased precipitation over the central Pacific (Fig. 1e). Interestingly, PC1 correlates closely ($r = 0.86$) with the independently derived GISS record of global MAMJ mean surface temperature (Fig. 1a).

The second PC time series (PC2) accounts for 16% of the variability among the 12 PC time series. This second mode represents ENSO variability (Fig. 2). Positive PC anomalies are associated with cold phase (La Niña) conditions. Negative anomalies are associated with warm phase (El Niño) conditions. Among ENSO indices, correlation is strongest ($r = -0.75$) with mean SST anomalies within the Niño-4 region (5°S – 5°N , 160°E – 150°W), calculated from the independently derived NOAA extended SST dataset (Fig. 2a). Although Niño-4 temperatures have warmed slightly in recent decades, Fig. 2a shows a slight (statistically insignificant) positive trend in the second PC time series toward cold phase conditions. While the NCEP/NCAR reanalysis precipitation data are known to be problematic (Janowiak et al. 1998), the first two PC time series were not impacted significantly by whether the precipitation data were included in the PCA.

The results of the PCA were not unique to the NCEP/NCAR reanalysis dataset. The same variables within the

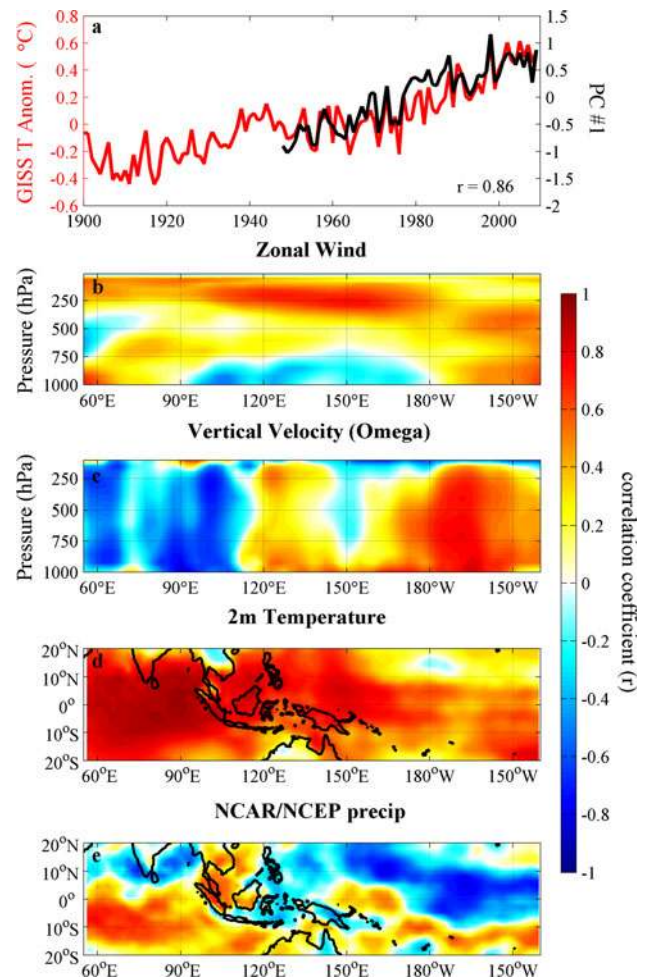


Fig. 1 a time series of PC 1 (black) and mean March–June GISS annual global temperature anomaly (red). Lower 4 panels: Correlation maps for regression of annual March–June climate on the PC 1 time series from (a). Climate variables are b mean zonal wind profile between 20°S and 20°N , c mean vertical velocity (ω) profile between 20°S and 20°N , d mean March–June temperature 2 m above sea level, and e NCEP/NCAR total precipitation. Values in c represent correlation with sinking motion, so cool colors represent correlations with rising motion, warm colors represent correlations with sinking motion

ECMWF ERA-40 dataset also produced very similar representations of these first two PC time series ($r = 0.88$ and 0.9 , respectively), despite coverage from only 1958 to 2002 (Fig. 3). Figure 3 shows that the first two PCs were also well represented within 1979–2009 radiosonde records of surface temperature and vertical profiles of zonal wind velocity. The shorter time scale of the radiosonde data, and thus diminished directional trends within records of temperature and wind velocity, caused the first and second PCs to be switched relative to the PC time series calculated from the longer reanalysis datasets. This was also the case when the PCA was replicated using only 1979–2009 NCEP/NCAR reanalysis surface temperature and zonal wind profile data (Fig. 3). A key difference between the

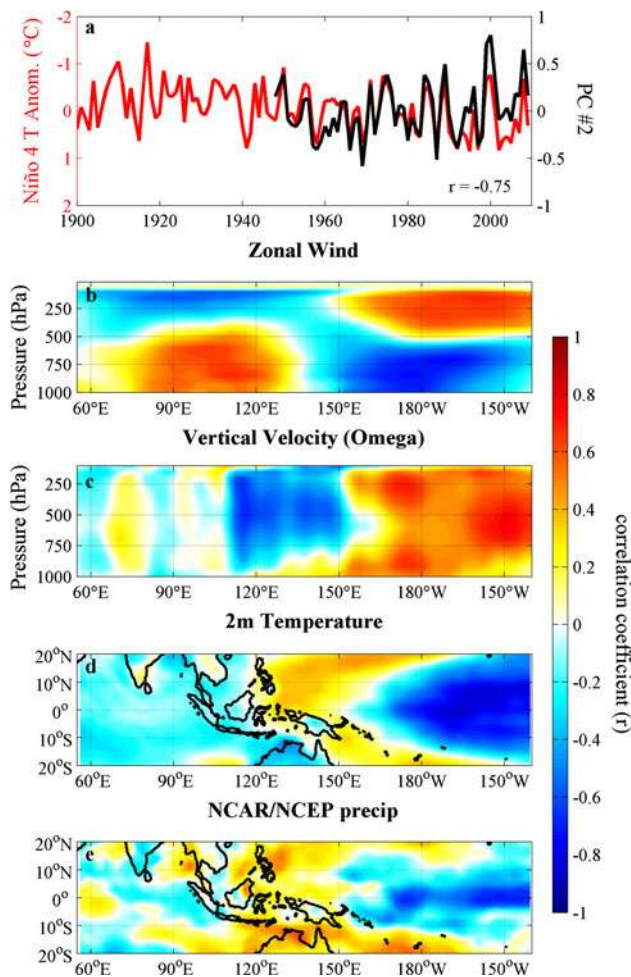


Fig. 2 a time series of PC 2 (black) and March–June mean Niño–4 temperature anomaly (red, inverted). Lower 4 panels are the same as in Fig. 1, but show correlation with PC 2

ECMWF ERA-40 and NCEP/NCAR reanalyses is that ECMWF indicates trends toward upward vertical velocity anomalies above the Indian and central Pacific Oceans while the NCEP/NCAR reanalysis shows upward anomalies above the Indian Ocean and downward anomalies above the central Pacific. We therefore only conclude that, as global temperatures have increased, convection has increased over the Indian Ocean during MAMJ. The central Pacific is substantially less instrumented and we remain skeptical regarding trends in central Pacific vertical velocities.

The mechanism underlying the positive trend in the first PC time series appears to be an extension of the western edge of the tropical warm pool in the Indian Ocean. Regressing smoothed 1900–2009 SST data with global mean temperatures (Fig. 4a) suggests that as tropical SSTs have increased globally, they have increased in the Indian Ocean two to three times faster

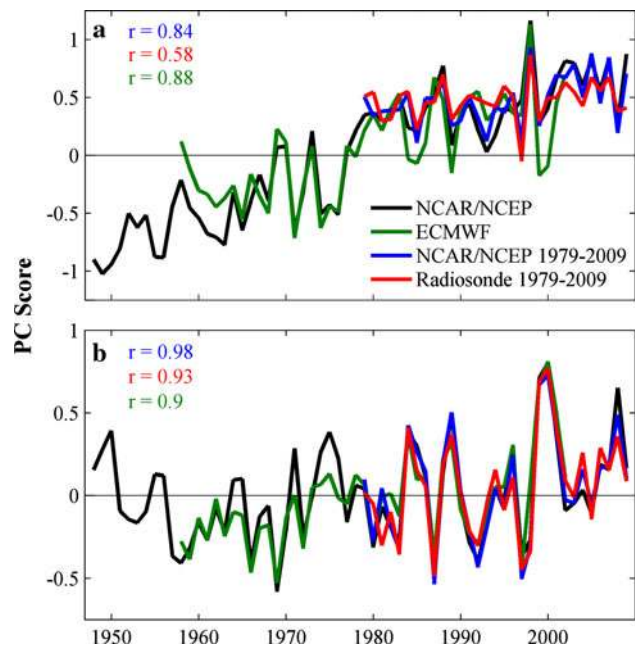


Fig. 3 Black and green lines represent a PC 1 and b PC 2 calculated using March–June NCEP/NCAR reanalysis data from 1948 to 2009 (also shown in Figs. 1 and 2) and ECMWF reanalysis from 1958 to 2002, respectively. Red lines are the first 2 PC time series calculated using March–June radiosonde 1,000 hPa temperature and profiles of zonal wind velocity from 1979 to 2009. Blue lines are the first 2 PC time series calculated using these same variables from the NCEP/NCAR reanalysis from 1979 to 2009. For PC time series calculated from 1979 to 2009, PC 2 appears in (a) and PC 1 appears in (b). *R* values indicate the correlation between the line of matching color and the black line

than SSTs in the tropical central Pacific (Fig. 4a). Figure 4b–c shows that the warm pool (here approximated as the area within the 28.75°C isotherm) has expanded by approximately 40° longitude on the west side of the warm pool in the past 50 years, from 100°E to 60°E. The majority of this expansion occurred dramatically in the 1960s and has been ongoing steadily since then. To the east, the 28.75°C isoline has expanded by approximately 20° (from 160°E to 180°E). The eastward expanse has been accompanied by much greater interannual and interdecadal variability due to ENSO. Over the past 5 years the eastern edge of the warm pool has had a similar position to that of the late 1980s and late 1990s. Figure 4d shows that, according to the NCEP/NCAR reanalysis, convective activity has increased over most of the warm pool region, especially on the western edge from 60°E to 90°E. In contrast, the NCEP/NCAR record shows a decrease in convective activity on the eastern edge of the warm pool immediately east of the dateline, consistent with the patterns shown in Fig. 1c. Particularly striking in both 4c and 4d is the dramatic post-1998 increase in both SSTs and convection over both the core

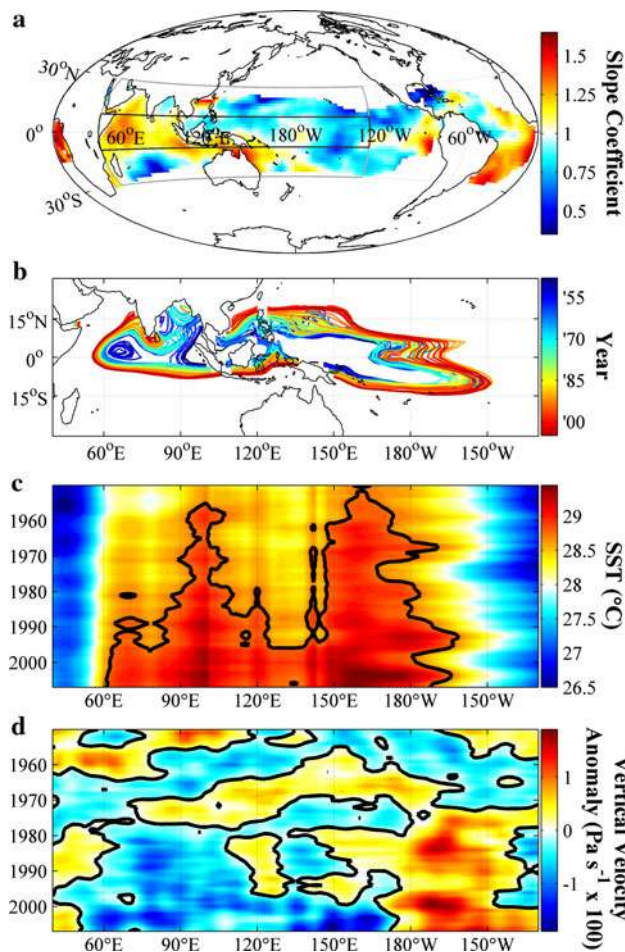


Fig. 4 **a** Change in March–June SST (NOAA extended reanalysis) versus change in global mean March–June surface temperature (GISS dataset). Slope coefficients are 7-years running mean SSTs regressed on 7-years running mean global temperature from 1900 to 2009. A slope of 1 indicates SST warming at the same pace as the global mean. Analysis was limited to regions where mean 1951–1980 March–June SST was $>24^{\circ}\text{C}$. Light and dark grey boxes bound the areas represented in (b) and (c–d), respectively. **b** Expansion of the warm pool from 1948 to 2009. Contours represent 5-years running 28.75°C isotherms. Warmer colored isotherms represent more recent 5-years periods. **c** and **d** Hovmöller plots of 5-years running mean March–June SST and 500 hPa vertical velocity (omega), respectively, between 10°S and 10°N . Black contours represent the 28.75°C isotherm in (c) and neutrality in (d). Negative values in (d) represent upward motion anomalies

of the Pacific warm pool ($\sim 150^{\circ}\text{E}$) and over the central Indian Ocean (60°E – 90°E).

3.2 Comparison of reanalysis to simulated and observed climate data

The disparity in SST warming rates between the tropical Indian and central Pacific Oceans is not accurately represented within the state-of-the-art GCMs used by the IPCC

AR4. Six observational datasets concur that for every degree increase in global temperatures, the tropical central Pacific increased by $\sim 0.5^{\circ}\text{C}$ and the tropical Indian Ocean increased by $\sim 1.5^{\circ}\text{C}$ (Fig. 5a). Comparing these results to those modeled by 21 GCMs in 84 model runs within the CMIP3 20c3m experiment, most models over predicted warming rates in the central Pacific Ocean by 200–300%. GCMs also generally over predicted the warming rate in the Indian Ocean, but not as severely (Fig. 5a). The tendency for GCMs to greatly over-estimate central Pacific surface warming relative to Indian Ocean warming may explain their tendency to slow the Pacific trade wind circulation, ultimately reducing transports of energy into the extra-tropics. The disparity between observations and CMIP3 results shown in Fig. 5a corresponds well with Hoerling et al. (2010), who show a similar discrepancy between the CMIP3 multi-model ensembles driven with greenhouse gas and aerosols, and 20th century multi-model ensembles driven with observed SST patterns. Models driven with observed SSTs exhibit a strengthened Walker circulation, and Hoerling et al. note that this overturning circulation has likely enhanced moisture transports across the Pacific, leading to moisture convergence and rainfall increases across parts of the warm pool.

Among the other variables evaluated, there is little GCM consensus on how conditions might have been impacted as global temperatures rose in the 20th century (Fig. 5b–d). Interestingly, the NCEP/NCAR and ECMWF reanalyses also disagree as to how zonal wind, vertical velocity, and precipitation have varied over the past half century over the sparsely instrumented central Pacific Ocean (Fig. 5b–d). Over the Indian Ocean, however, these reanalyses agree that convection and rainfall have increased in step with SSTs since the mid-1900s. While the NCEP/NCAR reanalysis suggest intensification of upper-level westerly anomalies above the eastern Indian Ocean and western Pacific Ocean, the ECMWF does not indicate a significant change in upper-level (or lower) zonal wind velocities in this region (Fig. 5b).

Given the disagreement among modeled and reanalysis datasets in how global temperatures relate to the overturning Walker circulation, it was important to validate that the PC time series presented in this paper represent true climate processes and not artifacts of the reanalysis parameterization and/or inputs. In particular, we were interested in whether other precipitation datasets reflect the positive relationship between PC1 and precipitation over the Indian Ocean that is apparent in the NCEP/NCAR and ECMWF reanalyses. This is important because we believe trends in precipitation over the tropical Indian Ocean should impact trends in east African long rains. To examine this question we examined the correlation between PC1 and Indian Ocean Precipitation (0°S – 15°S ,

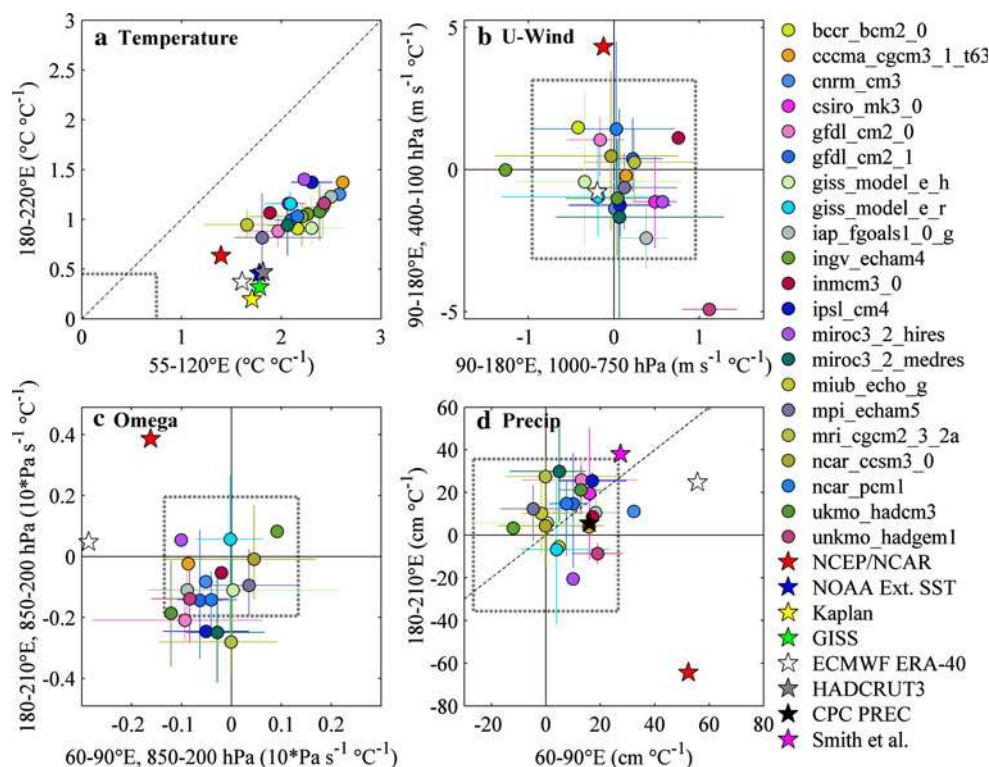


Fig. 5 Modeled and observed March–June relationships between global mean temperature and variables related to the tropical Indian-Pacific Ocean Walker Circulation. Relationships with global mean temperature are measured here as unit change per degree change in mean global temperature. Relationships were evaluated using data smoothed with a 5-years running mean to dampen the impact of high-frequency ENSO variability. Model and observed datasets cover various time scales within the period from 1948 to 2009. *Panel a* contrasts surface temperatures in the tropical Indian (10°N–10°S, 55°E–120°E) and central Pacific (10°N–10°S, 180°E–140°W). *Panel b* contrasts zonal wind velocity in the lower and upper troposphere in

the Indian-Pacific warm-pool area (10°N–10°S, 90°E–180°E). *Panel c* contrasts vertical velocity (omega) from 850 to 200 mb above the southern Indian Ocean (0°S–15°S, 60°E–90°E) and central Pacific (10°N–10°S, 180°E–150°W). *Panel d* contrasts total precipitation in the same regions represented in *panel (c)*. Circles model means. Vertical and horizontal lines running through circles of the same color: minimum and maximum of multiple runs. Stars Reanalysis and reconstructed data. Grey dashed boxes Unit change per °C given a correlation with global temperature of 0.3. Dashed diagonal lines in panels (a) and (d) are 1-to-1 lines

60°E–90°E) for each of the of the five validation precipitation datasets listed in Sect. 2.1. Considering 1979 through 2008 (the satellite era, during which we have relatively high confidence in ocean precipitation retrievals), PC1 correlated positively ($0.41 < r < 0.66$) and significantly ($10^{-6} < p < 0.03$) with all five data sets. In contrast, there was disagreement among the validation datasets regarding relationships with PC1 in the central Pacific Ocean, as was the case for NCEP/NCAR and ECMWF. PC2 was very well represented among the five validation datasets, with clear correlation patterns associated with ENSO (positive correlations over the Maritime Continent and negative correlations in the central Pacific).

It should be noted that the magnitude of the increases in latent heating shown by the various Indian Ocean rainfall observations ($\sim 30\text{--}50 \text{ cm } ^\circ\text{C}^{-1}$) is thermodynamically substantial. A 40 cm change in seasonal precipitation is equivalent to a 97 W m^{-2} flux, associated with a total of $3.58 \times 10^{14} \text{ W}$ across the associated region (0°S–15°S,

60°E–90°E). This is roughly 10% of the total latent heating across the entire tropical Indian Pacific (15°S–15°N, 60°E–80°W). It seems likely, therefore, that the $\sim 40^\circ$ geographic extension of the western border of the warm pool (Fig. 4b, c) has also influenced the warm pool thermodynamic circulation.

In summary, observational records and reanalysis products all show a dominant mode of climate variability in the tropical warm-pool area that is tightly coupled to global temperatures. Observational and reanalysis data also agree that the Indian Ocean's temperature response to global warming appears to be roughly three times that of the central Pacific's (Fig. 5a). The GCMs also show a greater rate of warming in the Indian versus Pacific, but overestimated warming in the central and eastern Pacific, causing the simulated gradients between Indian and Pacific SSTs to grow more slowly. Despite the fact that the observed gradients increased faster than simulated gradients, both observed and simulated records concur that the Indian

Ocean has warmed faster than the central Pacific. This suggests, in turn, that the differential heating rates may continue for some time to come. Another consensus among the observations and most models is the increase in rainfall across the Indian Ocean (Fig. 5d). The ECMWF agrees with the NCAR/NCEP reanalysis, suggesting that 1°C of global warming will be associated with increased convection and an increase of more than 50 cm of rainfall over the Indian Ocean during MAMJ. It seems safe to conclude that models and observations all concur on a positive correlation among global temperatures, Indian Ocean SSTs, and Indian Ocean rainfall.

What is uncertain is the atmospheric response to the warming signal over the central tropical Pacific. The NCEP/NCAR reanalysis shows a distinct overturning circulation, with increased ascent over the Indian Ocean coupled with subsidence across the central Pacific. This response, however, is not shown in the ECMWF reanalysis. Further, the CMIP3 models simulate a weak association between global temperatures and increased convection over both the central Pacific and Indian Oceans (Fig. 5c). The tendency for models to simulate an increase in convection over the central Pacific contributes to the popular interpretation that continued warming will lead to a more 'El Niño-like' climate. The strength of the correlations between modeled central Pacific vertical velocities and global temperatures, however, are weak (less than 0.4), so it is unclear how atmospheric circulation over the central Pacific will respond to continued warming and how these circulation changes will impact precipitation in regions where precipitation has been historically correlated with variability in ENSO indices.

3.3 Precipitation and circulation impacts of PC1 and PC2

As PC1 and global temperature have grown more positive and convection and rainfall have increased over the Indian Ocean in recent decades, precipitation totals during the long-rains season in eastern Africa have declined. In Ethiopia and Kenya, which are reasonably well instrumented with meteorological stations, our CHG-CLIM precipitation data indicate that declines have been most severe in the central and eastern regions (Fig. 6). In the last 30 years, MAMJ rainfall totals have declined by 35–45% of the 1950–1979 mean throughout much of the area to the south and east of the Ethiopian Highlands (Fig. 6b). The spatial characteristics and magnitude of these precipitation declines are corroborated by GPCP and GPCP data (Fig. 6a, c).

Figure 7 shows how long-season precipitation in eastern Africa and the leading modes of climate variability relate to moisture transports across the broad geographic region

studied in this paper. On average, large transports of moisture flow across the southern Indian Ocean and enter eastern Africa between 20°S and 20°N. Figure 7a indicates that the driest 20% of long-rains seasons have been associated with anomalously low specific humidity across equatorial east Africa, anti-cyclonic moisture transport anomalies across Ethiopia and northern Kenya, and divergence anomalies of moisture over the east coast of equatorial Africa and the western Indian Ocean. Dry seasons have also been associated with westerly moisture transport anomalies across the equatorial Indian Ocean and high specific humidity and convergence anomalies over much of the Maritime continent and southeastern Indian Ocean. In contrast, wet seasons have been characterized by approximately the opposite anomaly patterns (data not shown).

While the mean wind velocity and humidity data provided by the NCEP/NCAR reanalysis are too low in spatial resolution to accurately discern the complex paths of air parcels before reaching eastern Africa (Gatebe et al. 1999), the anomaly map in Fig. 7a suggests that the tropical Atlantic Ocean and Congo Basin may be important sources of water vapor for eastern Africa during MAMJ, consistent with Segele et al. (2009). During dry seasons, Walker circulation over the tropical Indian Ocean is particularly strong and the descending western branch of the cell appears to suppress moisture transports from the Atlantic, interior of Africa, and Indian Ocean (Fig. 7a). During wet seasons, moisture more freely converges upon eastern Africa and a weakened or eliminated descending branch of the Indian Ocean Walker circulation allows for increased convection and precipitation (data not shown).

The strength of the Indian Ocean Walker circulation is impacted by the ENSO cycle. The warm ENSO phase leads to a weaker Walker circulation and is weakly associated with enhanced long-rains precipitation in Kenya and Ethiopia. While correlations between long-rains precipitation and ENSO indices are weak, there is a strong association between low-level moisture convergence over the tropical warm pool and low-level divergence and dry conditions over eastern Africa (Fig. 7a). This contributes to the La Niña-like pattern in the map of dry anomalies in Fig. 7a, as can be seen by comparing Fig. 7a to a map of correlation between PC2 and vapor-transport, where the length of arrows depict the strength of correlation (Fig. 7c). Interestingly, ENSO indices have slightly trended toward a warmer phase in recent decades, but east African vapor transports and rainfall have declined. Figure 7b suggests that the decline of vapor transports into eastern Africa, despite the slight tilt toward warm-phase conditions, may be associated with rapid warming of the tropical Indian Ocean and a westward extension of the ascending branch of the Walker circulation (increasing PC1).

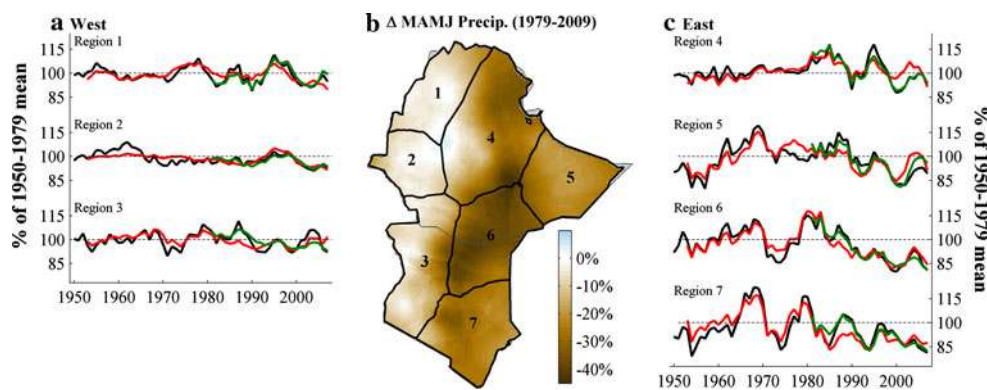


Fig. 6 **a** and **c** MAMJ regional, 5-years running average precipitation within Ethiopia and Kenya relative to the 1950–1979 mean. *Black lines* CHG-CLIM dataset, *red lines* GPPC, *green lines* GPCP. GPPC and GPCP records were linearly fit to the CHG-CLIM record. The numbered regions correspond to the regions outlined in **(b)**. **b** Change

in CHG-CLIM precipitation in the last 31 years relative to the 1950–1979 mean, calculated by linear regression. The seven regions were determined using a rotated principal components analysis. We did not consider locations where mean MAMJ precipitation <100 mm (*grey areas*) in any of these calculations

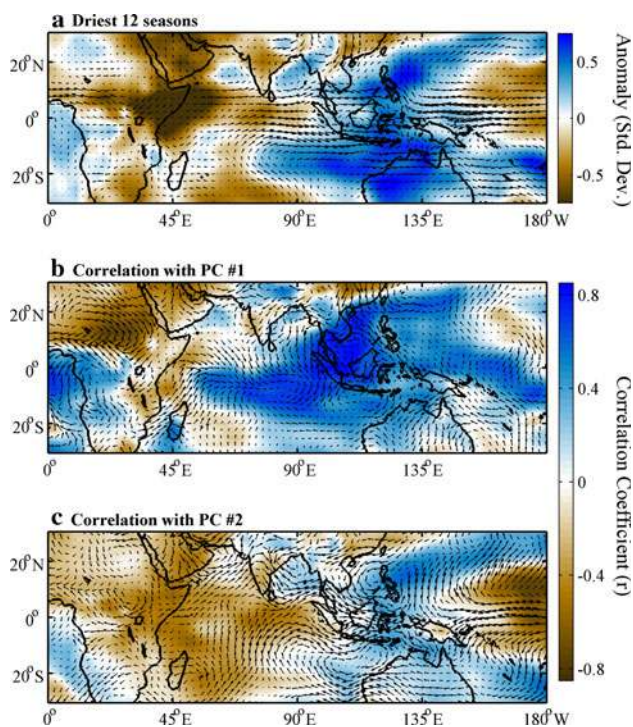


Fig. 7 MAMJ water–vapor transports (*arrows*) and precipitable water (*background*) in the lower troposphere (1,000–700 hPa). **a** Mean anomaly during the driest 12 MAMJ seasons from 1948 to 2009. **b** Correlation with PC1. **c** Correlation with PC2. MAMJ rainfall records were calculated using regions 6 and 7 in Fig. 6b

Viewing these relationships from a rotated perspective, Fig. 8a shows how PC1 correlates with vertical and zonal winds between 10°S and 10°N. Increased convergence and convection over the tropical Indian Ocean are associated with increased mid-level (~400–700 hPa) divergence aloft. Correlation arrows to the east of this divergence zone generally point upward and assimilate into a westerly correlation pattern associated with slowing of the tropical

easterly jet. Correlation arrows to the west continue west within the mid-level troposphere and descend toward the surface over the Sahara Desert. This subsidence pattern over the Sahara manifests itself in Fig. 7b as an anti-cyclonic flow pattern of dry air below 700 hPa. The eastern reach of this dry, anti-cyclonic correlation pattern comes across Sudan, Ethiopia, and Kenya, suggesting reduced vapor transports from the Atlantic Ocean and Congo Basin region to the west. Figures 7b and 8a also indicate reduced vapor transports from the Indian Ocean, as low-level winds over the western Indian Ocean have trended toward a low-level convergence pattern over the central Indian Ocean.

3.4 Relationship between PC1 and interannual variability

As was shown in Figs. 7b and 8a, PC1 manifests itself over tropical Africa and the Indian Ocean in a way that should impact the long rains. Using the correlation fields displayed in Fig. 8 as PC loadings, PC1 can be recalculated using zonal and vertical velocities over equatorial Africa and the Indian Ocean out to 120°E. The recalculated PC1 reflects how the circulation trends associated with the original PC1 impact climate across tropical Africa and the Indian Ocean. A 31-years running correlation between the recalculated PC1 and long-rains precipitation reveals a progressively more negative relationship over the past six decades, growing from $r \approx 0$ to $r \approx -0.45$ (not shown). This suggests that the manifestations of PC1 over Africa and the Indian Ocean are becoming increasingly influential on long-rains precipitation. Because these processes appear to have only a secondary influence on long rains totals, we were interested in identifying the primary atmospheric circulation factors related to long-rains precipitation and then determining whether the multi-decadal processes associated with PC1 have influenced these interannual relationships.

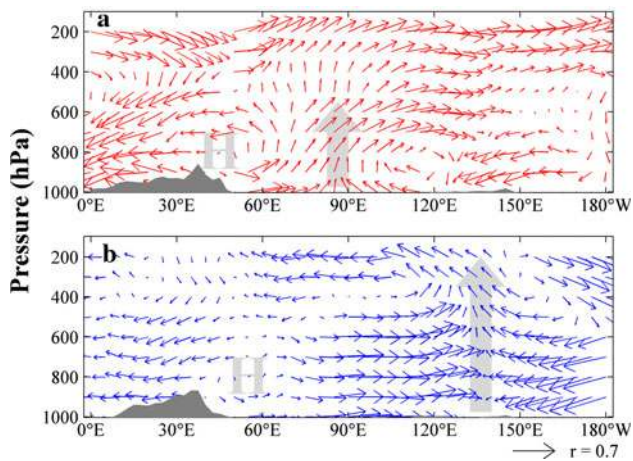


Fig. 8 Vertical profiles showing how tropical zonal and vertical circulation correlate with (a) PC1 and (b) PC2. **a** Zonal and vertical (omega) velocities were averaged across latitudes from 0°N to 20°N at longitudes west of, and including, 45°E. Velocities east of 45°E were averaged across latitudes from 20°S to 0°N. **b** Velocities were averaged across latitudes from 10°S to 10°N at all longitudes. Correlations with vertical velocity were multiplied by -1 so that *upward arrows* represent velocities away from the surface. *Dark grey areas* in the foreground represent average MAMJ surface pressure. *Thick grey arrows* in the background represent the zone of maximum correlation between the mode of climate variability and ascending atmospheric motion. The bold “H” in the background is for “high pressure” and represents the location of low-level divergence acting as the western source of return flow to the zone of convection

As discussed in Sect. 2.4, exploratory data analysis revealed a fairly simple circulation index (the MHG), based on 500 hPa geopotential heights (GPHs), that correlated well with East African rainfall at seasonal ($r = 0.61$) and multi-seasonal time-scales ($r = 0.74$ for 5-years running means). Wet years across eastern Africa are associated with decreased easterly flows aloft, and this pattern corresponds, in turn, to higher 500 hPa GPHs along the equator and lower 500 hPa GPHs across extra tropics (see Fig. 9a for boundaries of these regions). This pattern corresponds with the anomaly association associated with MJO activity (Pohl and Camberlin 2006a), but correlates better with east African rainfall throughout the 1948–2009 period than does MJO. Figure 9b plots seasonal MHG, MJO, and long-rains precipitation values. Figure 9c, d shows how vapor transports, zonal wind velocities, and vertical velocities correlate with MHG. High MHG years are associated with decreased convection over the Maritime continent, a weak tropical easterly jet across the Indian Ocean and Africa, increased moisture convergence and convection over eastern Africa, and increased moisture transports from the tropical Atlantic across central Africa. These are generally the same circulation characteristics associated with the MJO amplitude time series, but the MHG more explicitly represents the processes associated with long-rains precipitation.

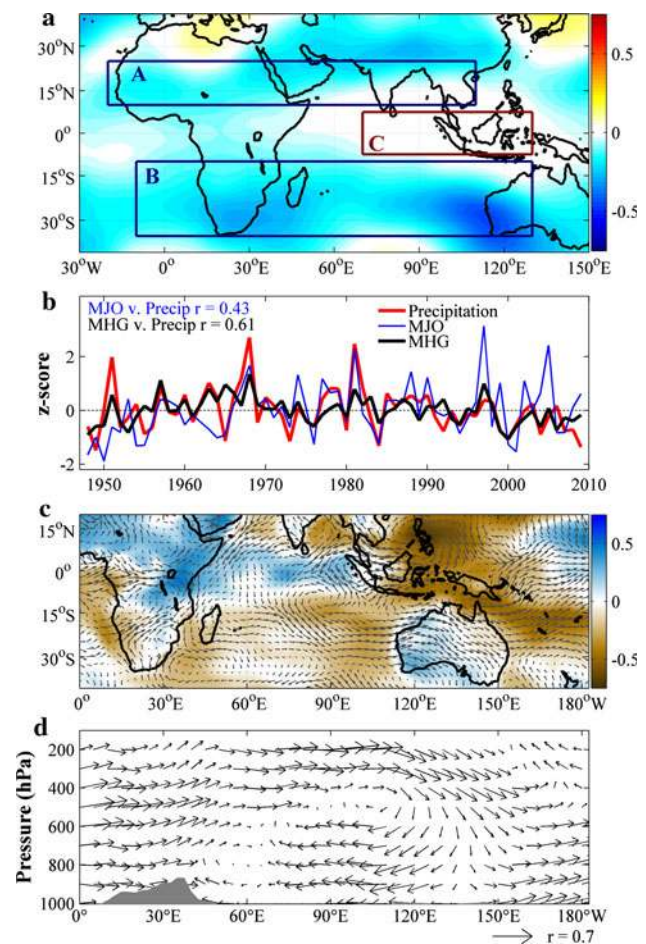


Fig. 9 **a** Correlation between 500-hPa geopotential height and long-rains precipitation. *Rectangles* bound the regions where geopotential heights are used to calculate the meridional height gradient (MHG). MHG values are highest when 500-hPa heights are low in the *blue rectangles* and high in the *red rectangles*. **b** Standardized time series of long-rains precipitation, MHG, and MJO amplitude. **c** Background shows correlation between the MHG and specific humidity integrated from 1,000 to 700 hPa. *Arrows* show directional correlation between MHG and vapor transport velocities. **d** Vertical profiles of correlation of the MHG with zonal and vertical (omega) wind velocities. Zonal and vertical velocities (omega) were averaged across latitudes from 10°S to 10°N. Correlations with vertical velocity were multiplied by -1 so that *upward arrows* represent upward velocities. *Dark grey areas* in the foreground represent average MAMJ surface pressure (land)

We evaluated the relative impacts of PC1 and MHG by considering composites of MAMJ precipitation during each of four classes of seasons: (1) Low PC1 High MHG, (2) High PC1 High MHG, (3) Low PC1 Low MHG, (4) High PC1 High MHG (Fig. 10). Composites calculated with GPCP and CHG-CLIM suggest that, which MHG has the primary impact on precipitation throughout the Horn of Africa, increases in PC1 have been associated with a tendency towards decreased precipitation in this region during both low and high MHG seasons. This tendency is only

moderate within Kenya’s coastal region (one of the two regions used to calculate the long-rains precipitation record used in this study) and much more pronounced inland.

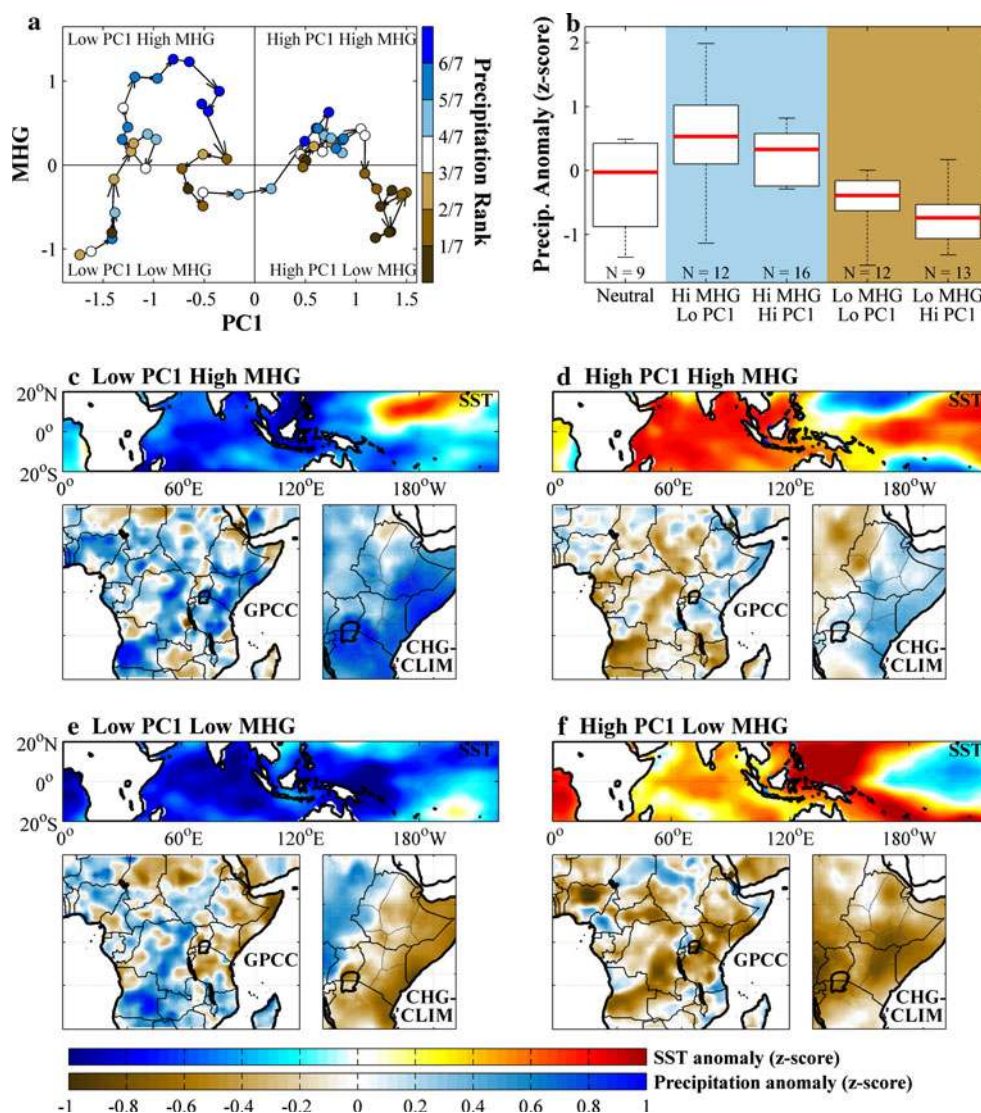
4 Discussion and conclusions

The PCA of reanalysis climate data indicated that the primary mode of variability within the tropical Indian Ocean has been strongly associated with increased global mean surface temperature and increased SST, convection, and rainfall in and above the Indian Ocean during MAMJ. These results are consistent with those of Goswami and Thomas (2000) and Minobe (2005). Both of these studies applied a PCA to global reanalysis data extending back to the late 1940s and also found that the first PC time series represents a long-term trend toward upward vertical velocity anomalies over the Indian Ocean and downward

anomalies over the central equatorial Pacific Ocean. Notably, the long-term increase observed by Goswami and Thomas reversed back to neutral in the mid 1990s, shortly before their climate reanalysis time series ended in 1996. In contrast, the time series used in the Minobe study extended through 2002 and the positive trend of PC1 was continuous throughout the record. Corroboration of this post-1940s trend toward anomalously rapid warming in the warm pool and Indian Ocean can be seen in the Indian-Pacific SST trends, especially once the ENSO signal has been removed (see Figure 9 in Compo and Sardeshmukh 2010).

While there is generally high confidence in temperature observations for most places on earth, there is much less confidence in the historical variability of precipitation, particularly over oceans. The validation test using five alternate reconstructions of global precipitation confirmed that indeed PC1 did correlate positively and significantly with Indian Ocean precipitation during the post-1979

Fig. 10 Impacts of PC1 and MHG on long-rains precipitation (long-term linear trend was removed from MHG to better isolate the interannual nature of variability). **a** Scatter plot of 5-years running standardized MHG versus standardized PC1. *Arrows* indicate direction in time. *Colors of circles* represent the rank of 5-years running long-rains precipitation totals, calculated with CHG-CLIM. *Each quadrant* shows a unique class of season based upon MHG and PC1. **b** *Box plot* of long-rains precipitation totals in five classes of seasons. Neutral seasons are seasons when MHG and/or PC1 were within 1/8 of a standard deviation from the mean. In all other classes, both variables were greater than 1/8 of a standard deviation from the mean. Maps (**c–f**) show a comparison of climate (SST and precipitation) anomalies during each of the four non-neutral classes. In each set of three maps, *top map* NOAA extended SST, *bottom-left map* GPCC precipitation, *bottom-right map* CHG-CLIM precipitation



satellite era. This offers confidence that PC1 represents a significant and large-scale trend in not only temperature, but also hydrologic processes throughout the Indian Ocean region. As an interesting note, a follow-up analysis revealed that the first PC of GPCP precipitation (1979–2009) within the original PCA region correlates well ($r = 0.75$) with the first PC time series calculated from 1948 to 2009 2-m temperature data, and poorly with the second temperature PC ($r = 0.28$). This was unexpected because, as Fig. 3 demonstrates, other datasets limited to 1979 onward are more representative of PC2 than they are of PC1 (as is the case with the CMAP precipitation dataset). Among the five validation records, GPCP is arguably the most trusted over tropical ocean regions (Yin et al. 2004), further emphasizing that convective activity and precipitation over the tropical Indian Ocean are very much linked with the surface temperature dynamics associated with PC1.

We interpret the strong and positive association between PC1 and MAMJ SSTs, convection, and rainfall within the tropical Indian Ocean region as a westward extension of the western, ascending branch of the tropical Walker circulation during MAMJ. This westward extension is clearly evident when comparing spatial mean fields of mid-tropospheric vertical velocities during the first half of the reanalysis period (1948–1978) to those of the second half (1979–2009; Fig. 11). Increased vertical ascent across the southern tropical Indian Ocean has been accompanied by decreased ascent over the central Pacific Ocean and parts of eastern Africa. Looking more closely at Africa, two changes appear noteworthy: (1) an increase in subsidence near the intersection of Somalia, Kenya and Ethiopia, and (2) a decrease in convection over parts of the Ethiopian highlands and Sudan. Both of these results support the findings of Funk et al. (2008): increased rainfall over the Indian Ocean is linked to (1) reduced onshore moisture transports into Kenya, Somalia and Ethiopia, and (2) ridging across tropical Africa that may enhance northerly flows out of the dry Sahara.

The westward extension of MAMJ Walker circulation appears to be partly driven by disproportionately rapid warming in the central and western Indian Ocean, which has effectively expanded the warm-pool region westward (Fig. 4). The westward expansion of the warm pool appears

to be a primary signature of increased global temperatures. Four SST datasets, two reanalysis products, and 21 CMIP3 models all indicate that Indian Ocean SSTs are tightly coupled with global temperatures during MAMJ (Fig. 5a); as global temperatures have increased since 1948, Indian Ocean SSTs have increased about 1.5 times as rapidly. These modeled and observational datasets also agree that SSTs in the tropical western and central Pacific are more weakly correlated with global temperatures during MAMJ, although models tend to over predict this relationship. Interestingly, regardless of whether they are constrained by actual 20th century SSTs, GCMs converge upon the projection of an increased Indian-Pacific SST gradient when they incorporate increased greenhouse forcing. This suggests that the increased SST gradient is anthropogenically driven (Barnett et al. 2005; Hoerling et al. 2010).

While the 21 GCMs evaluated in this study simulate a tilt toward more rapid warming in the Indian Ocean, they lack the substantial atmospheric Walker response above the Indian Ocean that is apparent in the reanalysis (Fig. 5b–d). Discrepancies between GCM simulations and reanalysis data within the tropics have been extensively documented (e.g., Santer et al. 2005, 2008; Soden et al. 2005; Karl et al. 2006; Mitras and Clement 2006; Douglass et al. 2008). Documented discrepancies generally regard trends in tropical lapse rates. While GCMs predict tropical lapse rates to decrease toward the moist adiabat (increased stability, weakened Hadley and Walker circulations, more ‘El Niño-like’), many observational records suggest the opposite. Recently, however, Santer et al. (2008) showed that, averaged throughout the tropics, the discrepancy between observed and modeled lapse rates is not statistically significant.

In the current study, we do not refute the modeled trends in mean lapse rate throughout the tropics, but we do challenge the idea that tropical climate is becoming more El Niño-like as the globe warms, at least over the Indian Ocean and eastern Africa during the MAMJ season. We suggest that, during this season, GCMs have generally overestimated the strength of the relationship between global mean temperatures and SSTs in the tropical central Pacific by a factor of two to three (Fig. 5a), thereby underestimating the SSTs contrast between the Indian Ocean and the central Pacific. As the SST gradient between the Indian Ocean and central Pacific has strengthened in step with global mean temperature, moisture convergence and convection have increased over the Indian Ocean. We suggest that this response to increasing global temperature is neither El Niño- nor La Niña-like, as is evidenced by the statistical independence of PC1, representing the westward expansion of the Walker circulation, and PC2, representing ENSO variability. Supporting this hypothesis, fossil corals in the tropical Pacific Ocean suggest that the mean state of

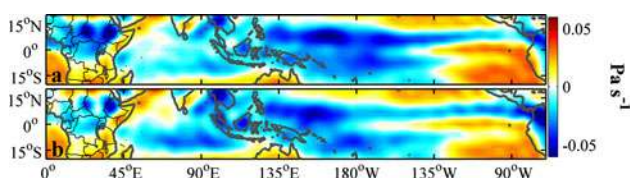


Fig. 11 Mean atmospheric vertical velocity during MAMJ between 700 and 400 hPa for **a** 1948–1978 and **b** 1979–2009. Cool shades indicate upward movement, warm shades indicate subsidence

ENSO and global temperatures have been uncorrelated for at least the past millennium (Cobb et al. 2003). Should global mean temperatures continue to rise beyond the realm of historical interannual variability, we expect that the gradient in SSTs between the warm tropical Indian Ocean and the relatively cooler Pacific Ocean will continue to increase in the near-term future. Du and Xie (2008) show that the differential warming rate is driven by the SSTs themselves: a given amount of warming causes relatively more evaporation from the already warmer Indian Ocean surface due to the exponential relationship between temperature and saturation vapor pressure. This local feedback mechanism likely accounts for the considerable coherence among CMIP3 estimates of increased air temperatures (Fig. 5a). The differential rates of evaporation lead to a more rapid increase in atmospheric water vapor over the warmer ocean surface, leading to enhanced greenhouse forcing and more warming. The specific mechanism of the warming feedback described by Du and Xie involves large increases in surface evaporation; these large increases in evaporation probably contribute to the coherent increases in rainfall over the tropical Indian Ocean (Funk et al. 2008). Further, greenhouse forcing should be more influential to the west of the cold-tongue region because forcing within the cold-tongue region is diluted by strong upwelling (Clement et al. 1996; Sun and Liu 1996; Cane et al. 1997; Seager and Murtugudde 1997). The disparate west versus east warming pattern could be exacerbated by a large-scale overturning circulation (Hoerling et al. 2010), advecting moisture into the Warm Pool region, and enhancing the water vapor feedback while simultaneously cooling the eastern Pacific via enhanced equatorial upwelling. Such an interpretation could be consistent with the observed trends (Fig. 4a).

Beyond the influence of the growing SST gradient, the westward extension of the MAMJ Walker circulation has also been fueled by increased diabatic heating above the Indian Ocean, associated with substantially increased convective cloud formation. Figure 12 shows that, according to satellite estimates of precipitation since 1979, PC1 is more strongly correlated with deep convective cloudiness over the central and western tropical Indian Ocean than anywhere else on Earth. It has been hypothesized that rapid Indian Ocean warming and subsequent convection should impact large-scale atmospheric circulation (Hoerling et al. 2004). In particular, increased cloud formation above the tropical Indian Ocean should cause large diabatic heating anomalies aloft and drive upper-level easterly anomalies toward the African coast and lower-level westerly moisture transport anomalies away from the African coast (Shanko and Camberlin 1998; Barlow et al. 2007; Funk et al. 2008). In these respects, our maps showing correlation between atmospheric circulation and

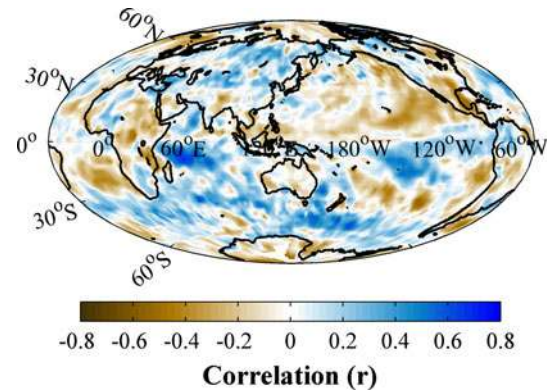


Fig. 12 Correlation between GPCP MAMJ rainfall totals and PC1 from 1979 to 2009

PC1 are strikingly similar (Figs. 7b, 8a). PC1 is strongly associated with reduced moisture transports from the Indian Ocean to the Horn of Africa. Additionally, while the increased easterly flow in the mid-troposphere has led to small subsidence anomalies over eastern Africa, it has led to larger subsidence anomalies over the Sahara region. Increased subsidence over the Sahara has led to increased low-level divergence in the region and a large anti-cyclonic circulation anomaly. Northeasterly anomalies along the eastern reach of this circulation and easterly anomalies to the south work to reduce moisture transports from the continental interior. Indeed, GPCP, GPCC, reanalysis, and the CHG-CLIM precipitation data all show a strong drying tendency along the western flank of the Highlands region of Ethiopia and Kenya during the past three decades. Further inland, moisture transports appear to have declined even more as PC1 has increased (Figs. 7b, 8a, 10c–f). While some inland regions impacted by the reduced moisture transports do not receive much precipitation during the MAMJ season anyway (e.g., Sudan), further reductions in moisture transports should have more serious impacts in parts of eastern Ethiopia (regions 1 and 2 in Fig. 6) where mean MAMJ precipitation exceeds 500 mm in many areas and summer precipitation (the dominant season) has already been declining for decades.

In summary, global surface temperatures are strongly correlated with Indian Ocean SSTs during MAMJ. As temperatures have increased, convection and precipitation above the Indian Ocean have increased and long-rains precipitation in eastern Africa has declined. This decline has been particularly strong on the eastern flank of the Ethiopian Highlands in Ethiopia and across central Kenya. Model simulations, driven by diabatic forcing over the southern Indian Ocean, suggest that increased convection and precipitation over the Indian Ocean are associated with a downwind reduction of low-level moisture transports toward eastern Africa (Funk et al. 2008). A similar process

has been implicated previously as a possible cause of drought in the African Sahel (Giannini et al. 2003). While most GCMs simulate a shift toward a more ‘El Niño-like’ climate in tropical eastern Africa in response to increasing global surface temperatures, we show that there is no evidence of increased El Niño-like conditions (somewhat increased rainfall) for MAMJ in eastern Africa during the period of observed anthropogenic warming of the last 40 years. This is at odds with the IPCC AR4 predictions of increased precipitation in tropical eastern Africa as a ‘likely’ response to anthropogenic global warming. While important regional variations such as the MHG will still produce wet seasons, we warn that long-rains precipitation has steadily declined over the past three decades. As this trend is associated with globally increasing temperatures, we estimate that even a GCM-projected mild shift toward more El Niño-like conditions would still be accompanied by an increased frequency of drought conditions in tropical eastern Africa due to reduced MAMJ rainfall. These findings are significant for adaptation planning for the region. Drier, rather than wetter conditions in the century ahead appear likely. The anthropogenic Indian Ocean warming response appears to be one of the most consistent (Hoerling et al. 2004; Barnett et al. 2005) and well understood (Du and Xie 2008) responses to greenhouse gas emissions. This anthropogenic warming appears to have already significantly altered the earth’s largest circulation feature and impacted its most food insecure inhabitants.

Acknowledgments This research was supported by the U.S. Agency for International Development Famine Early Warning System Network under U.S. Geological Survey Cooperative Agreement #G09AC00001 and the National Aeronautics and Space Administration under Precipitation Science Grant #NNX07AG266. We thank these agencies for their support. We also thank and acknowledge the CIMP3 modeling groups for providing data for analysis, and the World Climate Research Programme for collecting and archiving the model output. Thanks to Mingyue Chen and Tom Smith for help accessing global gridded precipitation reconstructions. Comments by Henry Diaz, Charles Jones, Joel Michaelsen, James Verdin, James Rowland, Kyle Cavanaugh, Greg Husak, Laura Harrison, Michael Marshall, Brian Osborn, and two anonymous reviewers greatly improved the quality of the manuscript.

Open Access This article is distributed under the terms of the Creative Commons Attribution Noncommercial License which permits any noncommercial use, distribution, and reproduction in any medium, provided the original author(s) and source are credited.

Appendix: Radiosonde data

Radiosondes measure atmospheric conditions from weather balloons and transmit them to fixed receivers on Earth. The radiosonde data used here came from the Integrated Global

Radiosonde Archive (IGRA) provided by the NOAA Satellite and Information Service (<http://www.ncdc.noaa.gov/oa/climate/igra/>). Radiosonde data represented individual soundings (not averages from multiple soundings). There are 93 radiosonde stations within the tropical Indian-Pacific Ocean area of 20°S–20°N, 55°E–140°W within the IRGA. The variables evaluated were temperature and zonal wind velocity. Temperature data were only considered at 1,000 mb. Zonal wind velocity data were considered at nine levels between 1,000 mb and 100 mb. Soundings are made twice-daily at 00:00 and 12:00 GMT. Radiosonde records often have data-gaps, so we consolidated data from the 93 stations into country-wide records. These 93 stations represent 31 countries. Before calculating country-wide records, we subjectively split stations within India into three well-agreeing sub-countries and stations within Thailand into two well-agreeing sub-countries, making for a total of 34 countries and sub-countries. We then determined that the temporal coverage of the data from stations in 15 of the countries and sub-countries was insufficient for inclusion in the PCA because the records were too short or had too many data gaps. The data records from the stations within the remaining 19 countries and sub-countries were nearly continuous from 1979 through 2009.

To conduct a PCA on multiple decades of raw MAMJ data, we filled missing observational data with downscaled 3-h NCEP/NCAR reanalysis data. At each station, for each variable, at each sounding time (00:00 and 12:00 GMT), and for each month within the MAMJ season, we used linear regression between radiosonde observational data and reanalysis data to downscale reanalysis data to best represent daily conditions at sounding sites. After filling the data gaps, data collected at 00:00 GMT and 12:00 GMT were then converted to z-scores at each station and averaged together to create station-specific *daily* records for each variable. The 122 daily records from each MAMJ season were then averaged together to create a mean seasonal record at each station. Each seasonal record was converted to z-scores and the standardized seasonal records were averaged across all stations within each of the 19 countries and sub-countries. We limited our analysis to 1979 and beyond because (1) radiosonde data within the 19 countries and sub-countries were less common before 1979 and (2) reanalysis data are presumably less representative of true sub-daily atmospheric conditions during the pre-satellite era.

References

- Abram NJ, Gagan MK, Cole JE, Hantoro WS, Mudelsee M (2008) Recent intensification of tropical climate variability in the Indian Ocean. *Nat Geosci* 1:849–853

- Adler RF, Susskind J, Huffman GJ et al (2003) The version-2 global precipitation climatology project (GPCP) monthly precipitation analysis (1979–present). *J Hydromet* 4:1147–1167
- Barlow M, Hoell A, Colby F (2007) Examining the wintertime response to tropical convection over the Indian Ocean by modifying convective heating in a full atmospheric model. *Geophys Res Lett* 34:L19702
- Barnett TP, Pierce DW, AchutaRao KM, Gleckler PJ, Santer BD, Gregory JM, Washington WM (2005) Penetration of human-induced warming into the world's oceans. *Science* 309:284–287
- Camberlin P, Philippon N (2002) The east African March–May rainy season: associated atmospheric dynamics and predictability over the 1968–1997 period. *J Climate* 15:1002–1019
- Cane MA, Clement AC, Kaplan A et al (1997) Twentieth-century sea surface temperature trends. *Science* 275:957–960
- Chen J, Carlson BE, Del Genio AD (2002) Evidence for strengthening of the tropical general circulation in the 1990s. *Science* 295:838–841
- Christiansen JH, Hewitson A, Busuioc A et al (2007) Regional climate projections, ch. 11. In: Solomon S, Qin D, Manning M et al (eds) *Climate change 2007: the physical science basis, contribution of working group I to the fourth assessment report of the intergovernmental panel on climate change*. Cambridge University Press, Cambridge, pp 849–940
- Clement A, Seager R, Cane MA, Zebiak SE (1996) An ocean dynamical thermostat. *J Climate* 9:2190–2196
- Cobb KM, Charles CD, Cheng H, Edwards RL (2003) El Niño/Southern oscillation and tropical Pacific climate during the last millennium. *Nature* 424:271–276
- Compo GP, Sardeshmukh PD (2010) Removing ENSO-related variations from the climate record. *J Climate*. doi:10.1175/2009JCLI2735.1
- Diaz HF, Markgraf V (1992) *El Niño: historical and paleoclimatic aspects of the southern oscillation*. Cambridge University Press, Cambridge
- Dinku T, Connor SJ, Ceccato P, Ropelewski CF (2008) Comparison of global gridded precipitation products over a mountainous region of Africa. *Int J Climatol* 28:1627–1638
- Douglass DH, Christy JR, Pearson BD, Singer SF (2008) A comparison of tropical temperature trends with model predictions. *Int J Climatol* 28:1693–1701
- Du Y, Xie SP (2008) Role of atmospheric adjustments in the tropical Indian Ocean warming during the 20th century in climate models. *Geophys Res Lett* 35:391–405
- Funk CC, Brown ME (2009) Declining global per capita agricultural production and warming oceans threaten food security. *Food Sec* 1:271–289
- Funk C, Michaelsen J (2004) A simplified diagnostic model of orographic rainfall for enhancing satellite-based rainfall estimates in data-poor regions. *J Appl Meteorol* 43:1366–1378
- Funk C, Verdin J (2003) Comparing satellite rainfall estimates and reanalysis precipitation fields with station data for western Kenya. In: Dijkstra D, Rembold F, Nègre T et al (eds) *Proceedings of the JRC–FAO international workshop*. European Commission, Nairobi
- Funk C, Verdin JP (2009) Real-time decision support systems: the famine early warning system network. In: Gebremichael M, Hossain F (eds) *Satellite rainfall applications for surface hydrology*. Springer, Netherlands, pp 295–320
- Funk C, Michaelsen J, Verdin J et al (2003) The collaborative historical African rainfall model: description and evaluation. *Int J Climatol* 23:47–66
- Funk C, Senay G, Asfaw A et al (2005) Recent drought tendencies in Ethiopia and equatorial-subtropical eastern Africa. US Agency for International Development, Washington
- Funk C, Husak G, Michaelsen J, Love T, Pedreros D (2007) Third generation rainfall climatologies: satellite rainfall and topography provide a basis for smart interpolation. In: *Proceedings of the JRC–FAO Workshop*, Nairobi, Kenya
- Funk CC, Dettinger MD, Michaelsen JC, Verdin JP, Brown ME, Barlow M, Hoell A (2008) Warming of the Indian Ocean threatens eastern and southern African food security but could be mitigated by agricultural development. *Proc Nat Acad Sci USA* 105:11081–11086
- Gatebe CK, Tyson PD, Annegarn H, Piketh S, Helas G (1999) A seasonal air transport climatology for Kenya. *J Geophys Res* 104:14237–14244
- Giannini A, Saravanan R, Chang P (2003) Oceanic forcing of Sahel rainfall on interannual to interdecadal time scales. *Science* 302:1027–1030
- Gill AE (1980) Some simple solutions for heat-induced tropical circulation. *Q J Roy Meteor Soc* 106:447–462
- Gill AE (1982) *Atmosphere-ocean dynamics*, vol 30. Academic Press, San Diego
- Goswami BN, Thomas MA (2000) Coupled ocean-atmosphere interdecadal modes in the tropics. *J Meteorol Soc Jpn* 78:765–775
- Graham NE (1994) Decadal-scale climate variability in the tropical and North Pacific during the 1970s and 1980s: observations and model results. *Clim Dynam* 10:135–162
- Hastenrath S, Nicklis A, Greischar L (1993) Atmospheric-hydro-spheric mechanisms of climate anomalies in the western equatorial Indian Ocean. *J Geophys Res* 98:20219
- Held IM, Soden BJ (2006) Robust responses of the hydrological cycle to global warming. *J Climate* 19:5686–5699
- Hoerling MP, Hurrell JW, Xu T, Bates GT, Phillips AS (2004) Twentieth century North Atlantic climate change. Part II: understanding the effect of Indian Ocean warming. *Clim Dyn* 23:391–405
- Hoerling M, Eischeid J, Perlwitz J (2010) Regional precipitation trends: distinguishing natural variability from anthropogenic forcing. *J Climate* 23:2131–2145
- Huffman GJ, Adler RF, Arkin P et al (1997) The global precipitation climatology project (GPCP) combined precipitation dataset. *Bull Amer Meteor Soc* 78:5–20
- Huffman GJ, Adler RF, Bolvin DT, Gu G (2009) Improving the global precipitation record: GPCP version 2.1. *Geophys Res Lett* 36:L17808
- Janowiak JE, Gruber A, Kondragunta CR, Livezey RE, Huffman GJ (1998) A comparison of the NCEP–NCAR reanalysis precipitation and the GPCP rain gauge—satellite combined dataset with observational error considerations. *J Climate* 11:2960–2979
- Kanamitsu M, Ebisuzaki W, Woollen J, Yang SK, Hnilo JJ, Fiorino M, Potter GL (2002) NCEP–DOE AMIP-II reanalysis (R-2). *Bull Amer Met Soc* 83:1631–1643
- Karl TR, Hassol SJ, Miller CD, Murray WL (eds) (2006) *Temperature trends in the lower atmosphere: steps for understanding and reconciling differences*. US Government, Washington
- Kirtman BP, Schopf PS (1998) Decadal variability in ENSO predictability and prediction. *J Climate* 11:2804–2822
- Knutson TR, Manabe S (1995) Time-mean response over the tropical Pacific to increased CO₂ in a coupled ocean-atmosphere model. *J Climate* 8:2181–2199
- Lu J, Vecchi GA, Reichler T (2007) Expansion of the Hadley cell under global warming. *Geophys Res Lett* 34. doi:10.1029/2006GL028443
- Madden RA, Julian PR (1971) Detection of a 40–50 day oscillation in the zonal wind in the tropical Pacific. *J Atmos Sci* 28:702–708
- Madden RA, Julian PR (1972) Description of global-scale circulation cells in the tropics with a 40–50 day period. *J Atmos Sci* 29:1109–1123

- Madden RA, Julian PR (1994) Observations of the 40–50-day tropical oscillation—a review. *Mon Weath Rev* 122:814–837
- Meehl GA, Stocker TF, Collins WD et al (2007) Global climate projections, ch. 10. In: Solomon S, Qin D, Manning M et al (eds) *Climate change 2007: the physical science basis, contribution of working group I to the fourth assessment report of the intergovernmental panel on climate change*. Cambridge University Press, Cambridge, pp 749–845
- Minobe S (2005) Year-to-year variability in the Hadley and Walker circulations from NCEP/NCAR reanalysis data. In: Diaz HF, Bradley RS (eds) *The Hadley circulation: present, past and future*. Kluwer Academic Publishers, Netherlands, pp 153–171
- Mitas CM, Clement A (2006) Recent behavior of the Hadley cell and tropical thermodynamics in climate models and reanalyses. *Geophys Res Lett* 33:1810–1813
- Nicholson SE, Kim J (1997) The relationship of the El Niño–Southern oscillation to African rainfall. *Int J Climatol* 17:117–135
- Nicholson SE, Selato JC (2000) The influence of La Niña on African rainfall. *Int J Climatol* 20:1761–1776
- Ogallal LJ (1988) Relationships between seasonal rainfall in East Africa and the Southern Oscillation. *Int J Climatol* 8:31–43
- Pohl B, Camberlin P (2006a) Influence of the Madden-Julian Oscillation on East African rainfall. I: intraseasonal variability and regional dependency. *Q J Roy Met Soc* 132:2521–2539
- Pohl B, Camberlin P (2006b) Influence of the Madden-Julian Oscillation on East African rainfall: II. March–May season extremes and interannual variability. *Q J Roy Meteor Soc* 132:2541–2558
- Preisendorfer RW, Zwiers FW, Barnett TP (1981) Foundations of principal components selection rules. In: SIO reference series, vol 81. Scripps Institution of Oceanography, La Jolla, CA, USA, p 4
- Quan XW, Diaz HF, Hoerling MP (2004) Change in the tropical Hadley cell since 1950. In: Diaz HF, Bradley RS (eds) *The Hadley circulation: past, present and future*. Kluwer Academic Publishers, Netherlands, pp 85–120
- Randall DA, Wood RA, Bony S et al (2007) Climate models and their evaluation, ch. 8. In: Solomon S, Qin D, Manning M et al (eds) *Climate change 2007: the physical science basis, contribution of working group I to the fourth assessment report of the intergovernmental panel on climate change*. Cambridge University Press, Cambridge, pp 589–662
- Rowell DP, Ininda JM, Ward MN (1994) The impact of global sea surface temperature patterns on seasonal rainfall in East Africa. In: *Proceeding of international conference monsoon variability and prediction*, vol 619. WMO, Trieste, Italy, pp 9–13
- Saji NH, Goswami BN, Vinayachandran PN, Yamagata T (1999) A dipole mode in the tropical Indian Ocean. *Nature* 401:360–363
- Santer BD, Wigley TML, Mears C et al (2005) Amplification of surface temperature trends and variability in the tropical atmosphere. *Science* 309:1551–1556
- Santer BD, Thorne PW, Haimberger L et al (2008) Consistency of modelled and observed temperature trends in the tropical troposphere. *Int J Climatol* 28:1703–1722
- Seager R, Murtugudde R (1997) Ocean dynamics, thermocline adjustment, and regulation of tropical SST. *J Climate* 10:521–534
- Segele ZT, Lamb PJ, Leslie LM (2009) Seasonal-to-interannual variability of Ethiopian/Horn of Africa Monsoon. Part I: associations of wavelet-filtered large-scale atmospheric circulation and global sea surface temperature. *J Climate* 22:3396–3421
- Shanko D, Camberlin P (1998) The effects of the Southwest Indian Ocean tropical cyclones on Ethiopian drought. *Int J Climatol* 18:1373–1388
- Smith TM, Arkin PA, Sapiano MRP, Chang C-Y (2010) Merged statistical analyses of historical monthly precipitation anomalies beginning 1900. *J Climate* 23:5755–5770
- Soden BJ, Jackson DL, Ramaswamy V, Schwarzkopf MD, Huang X (2005) The radiative signature of upper tropospheric moistening. *Science* 310:841–844
- Solomon S, Qin D, Manning M et al (2007) *Climate change 2007: contribution of working group I to the fourth assessment report of the intergovernmental panel on climate change*. Cambridge University Press, Cambridge
- Sun D-Z, Liu Z (1996) Dynamic ocean-atmosphere coupling, a thermostat for the tropics. *Science* 272:1148–1150
- Vecchi GA, Soden BJ (2007) Global warming and the weakening of the tropical circulation. *J Climate* 20:4316–4340
- Vecchi GA, Soden BJ, Wittenberg AT, Held IM, Leetmaa A, Harrison MJ (2006) Weakening of tropical Pacific atmospheric circulation due to anthropogenic forcing. *Nature* 441:73–76
- Verdin J, Funk C, Senay G, Choularton R (2005) Climate science and famine early warning. *Philos T Roy Soc B* 360:2155–2168
- von Storch H, Zwiers FW (1999) *Statistical analysis in climate research*, vol 1. Cambridge University Press, New York
- Webster PJ (1998) Monsoons—processes, predictability, and the prospects for prediction. *J Geophys Res* 103:14451–14510
- Wheeler MC, Hendon HH (2004) An all-season real-time multivariable MJO index: development of an index for monitoring prediction. *Mon Weath Rev* 132:1917–1932
- Xie P, Arkin PA (1997) Global precipitation: a 17-years monthly analysis based on gauge observations, satellite estimates, and numerical model outputs. *Bull Amer Met Soc* 78:2539–2558
- Yin X, Gruber A, Arkin P (2004) Comparison of the GPCP and CMAP merged gauge-satellite monthly precipitation products for the period 1979–2001. *J Hydrometeor* 5:1207–1222
- Zhang Y, Wallace JM, Battisti DS (1997) ENSO-like interdecadal variability: 1900–1993. *J Climate* 10:1004–1020